Supplementary Material

Global increase in the optimal temperature for the productivity of terrestrial ecosystems

Zhongxiang Fang[1], Wenmin Zhang[1], Lanhui Wang[2, 3], Guy Schurgers[1], Philippe Ciais[4], Josep Peñuelas[5], Martin Brandt[1], Hui Yang[6], Ke Huang[1], Qiu Shen[7], and Rasmus Fensholt[1]

[1]Department of Geosciences and Natural Resource Management, University of Copenhagen, Øster Voldgade 10, DK-1350 Copenhagen, Denmark.

[2]Center for Biodiversity Dynamics in a Changing World (BIOCHANGE) and Section for Ecoinformatics & Biodiversity, Department of Biology, Aarhus University, Ny Munkegade 114, 8000, Aarhus C, Denmark.

[3]Department of Physical Geography and Ecosystem Science, Lund University, Sölvegatan 12, SE- 223 62 Lund, Sweden.

[4]Laboratoire des Sciences du Climat et de l'Environnement, CEA CNRS UVSQ, Gif-sur-Yvette, France.

[5]CSIC, Global Ecology Unit CREAF-CEAB-UAB, Cerdanyola del Vallès, 08193, Catalonia, Spain.

[6]Department for Biogeochemical Integration, Max-Planck-Institute for Biogeochemistry, 07745 Jena, Germany

[7]Faculty of Geographical Science, Beijing Normal University, Beijing 100875, China.

Table of Contents

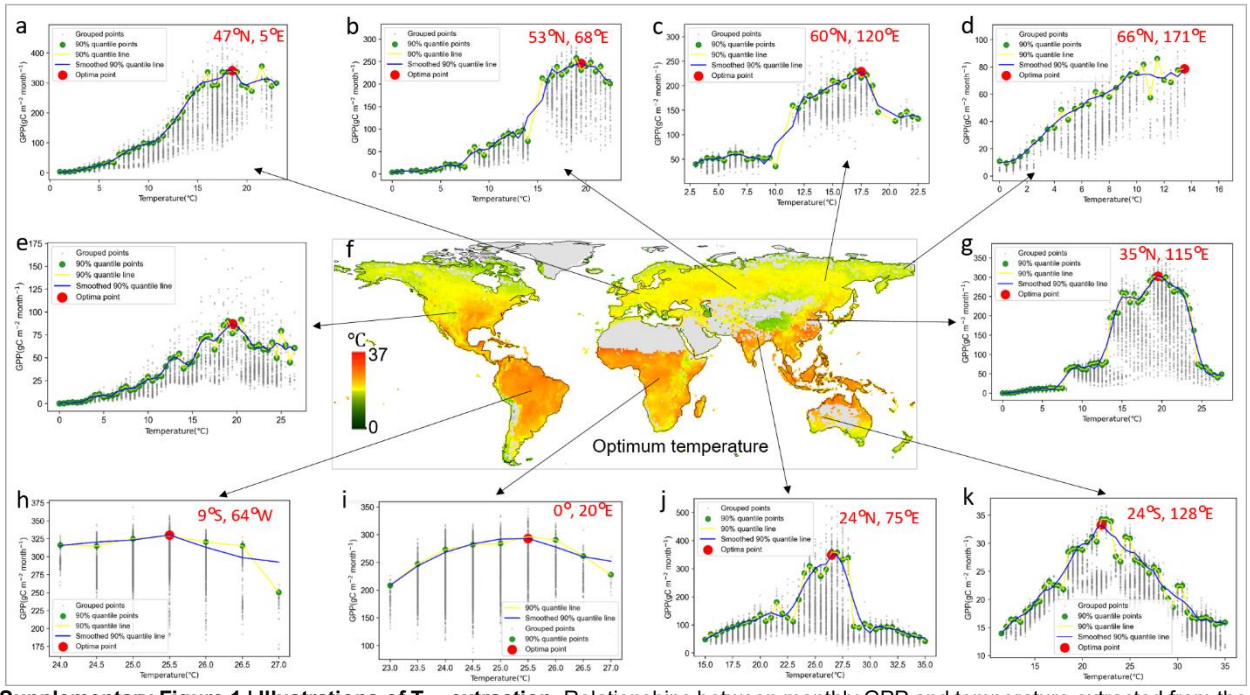

Supplementary Figure 1 | Illustrations of T_{opt} extraction. Relationships between monthly GPP and temperature extracted from the first 5-y temporal window (1982-1986) at a 1° spatial window. The map shows the locations of the selected sample plots. Panel d represents an example where T_{opt} could not be retrieved as T_{opt} was located at the end of the curve. The remaining figures are examples from around the globe, where T_{opt} could effectively be retrieved.

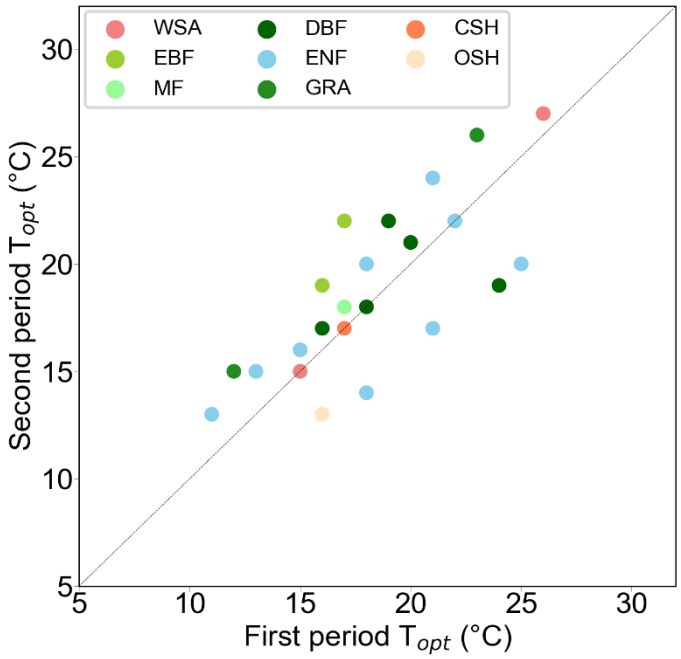

Supplementary Figure 2 | Optimal temperature in two different 5-year periods: 2001-2005 and 2010-2014 for different ecosystems. The optimal temperature is derived from the daily FLUXNET sites observations using a 5-y temporal window for 2001-2005 and 2010-2014. Different colors of the points indicate different ecosystems according to IGBP classification. CSH, Closed Shrublands; DBF, Deciduous Broadleaf Forests; EBF, Evergreen Broadleaf Forests; ENF, Evergreen Needleleaf Forests; GRA, Grasslands; MF, Mixed Forests; OSH, Open Shrublands; WSA, Woody Savannas.

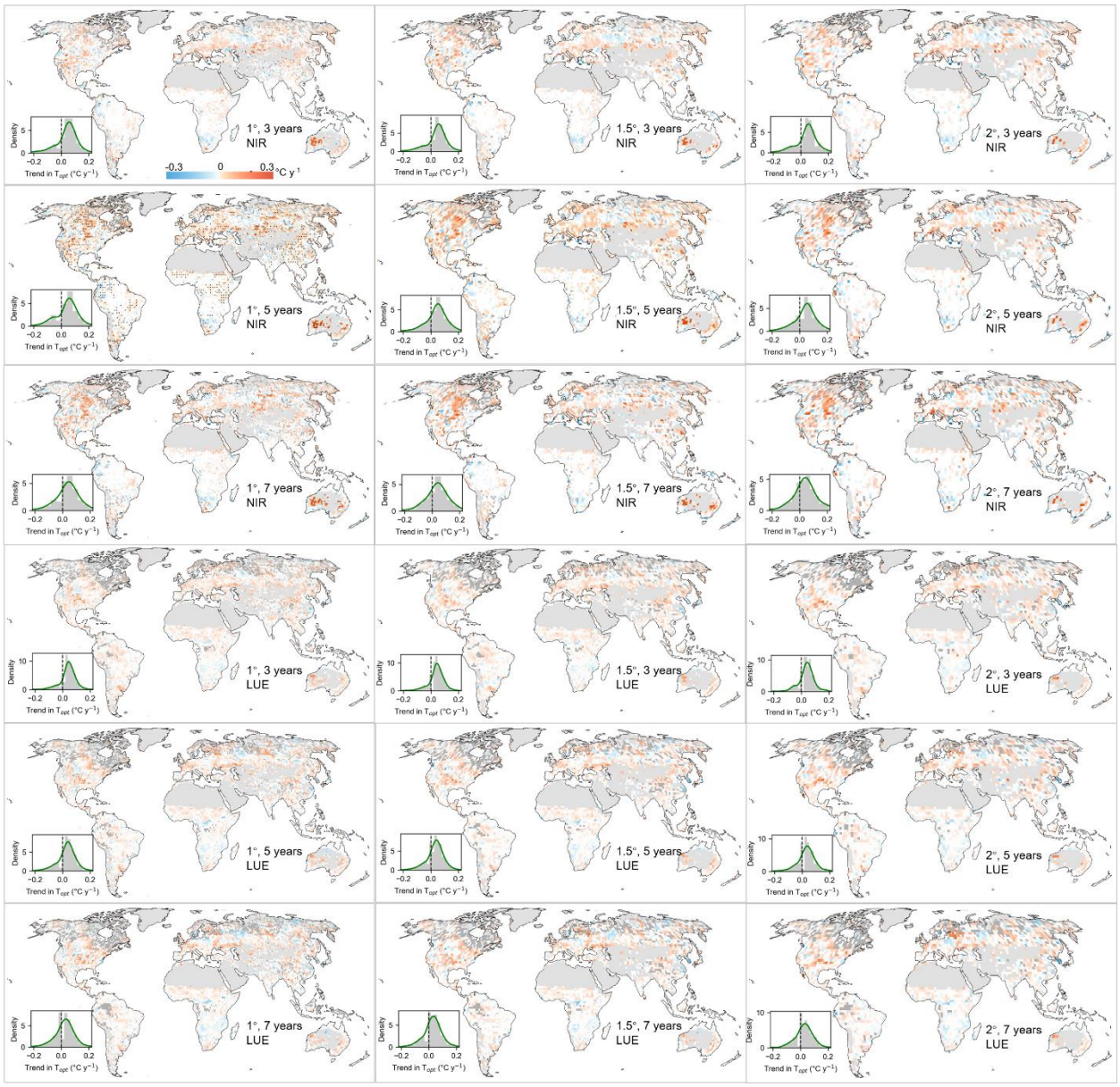

Supplementary Figure 3 | Spatial patterns of trends in T_{opt} using different combinations of sizes of spatial and temporal windows for 1982-2016. Temporal windows of 3, 5, and 7 years were tested to calculate T_{opt}, and the sizes of the spatial windows were 1, 1.5, and 2°. Light gray indicates areas with sparse or no vegetation, and dark gray indicates areas where T_{opt} could not be successfully retrieved (see Methods).

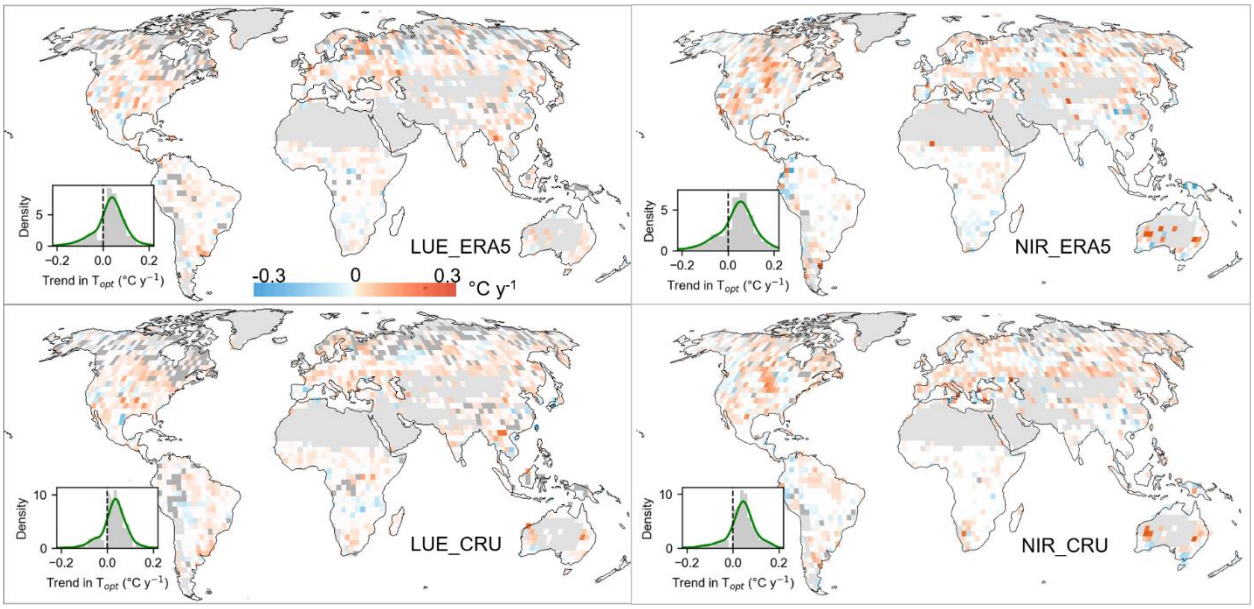

Supplementary Figure 4 | Spatial patterns of trends in T_{opt} with a 5-y temporal window and a 2.5° spatial window for 1982-2016 based on different data sets. NIR GPP and LUE GPP are independent GPP data sets, and ERA5 and CRU are independent temperature data sets. Light gray indicates areas with sparse or no vegetation, and dark gray indicates areas where T_{opt} could not be successfully retrieved (see Methods).

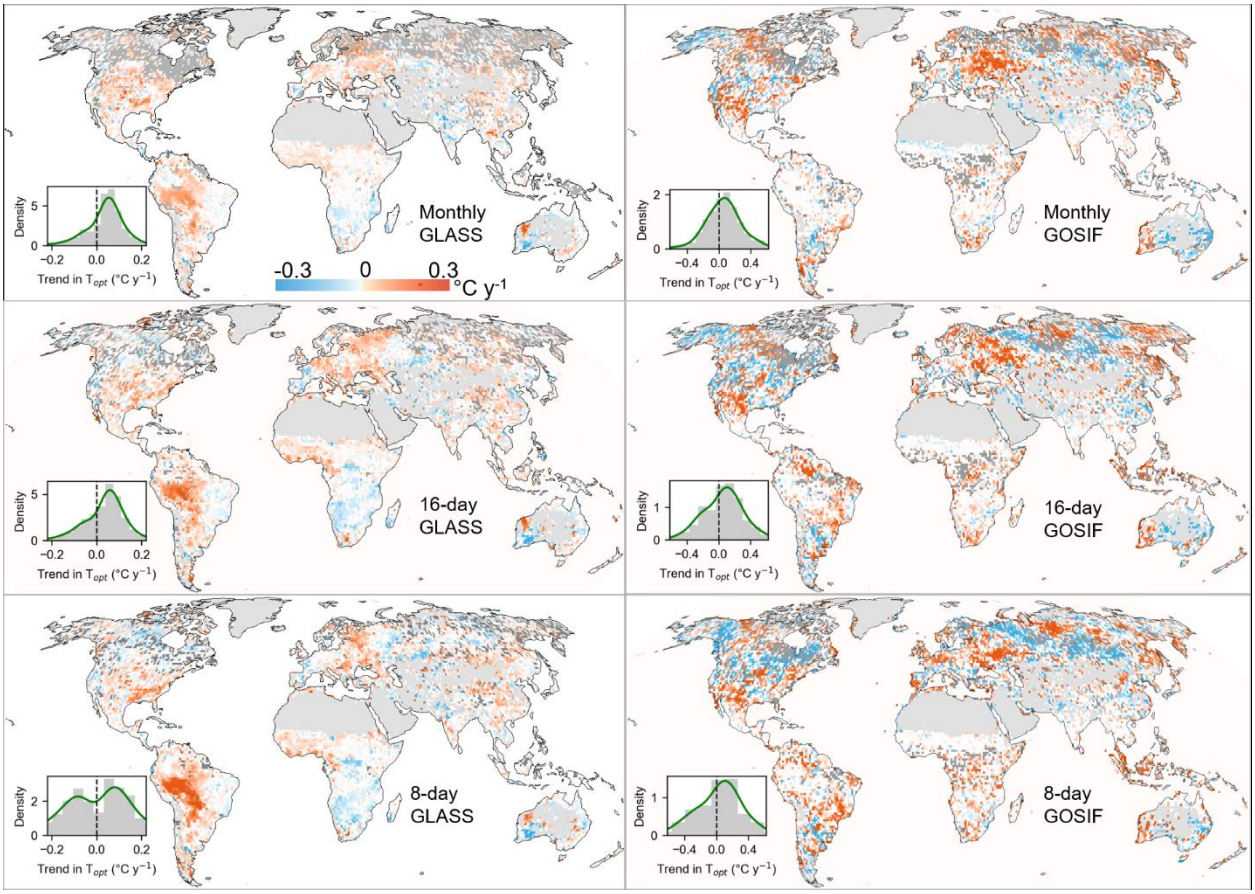

Supplementary Figure 5 | Spatial patterns of trends in T_{opt} with a 5-y temporal window and a 1° spatial window for 1982-2016 based on different temporal composition of GLASS GPP data sets and for 2001 to 2016 based on different temporal composition of GOSIF GPP data sets, respectively. Light gray indicates areas with sparse or no vegetation, and dark gray indicates areas where T_{opt} could not be successfully retrieved (see Methods).

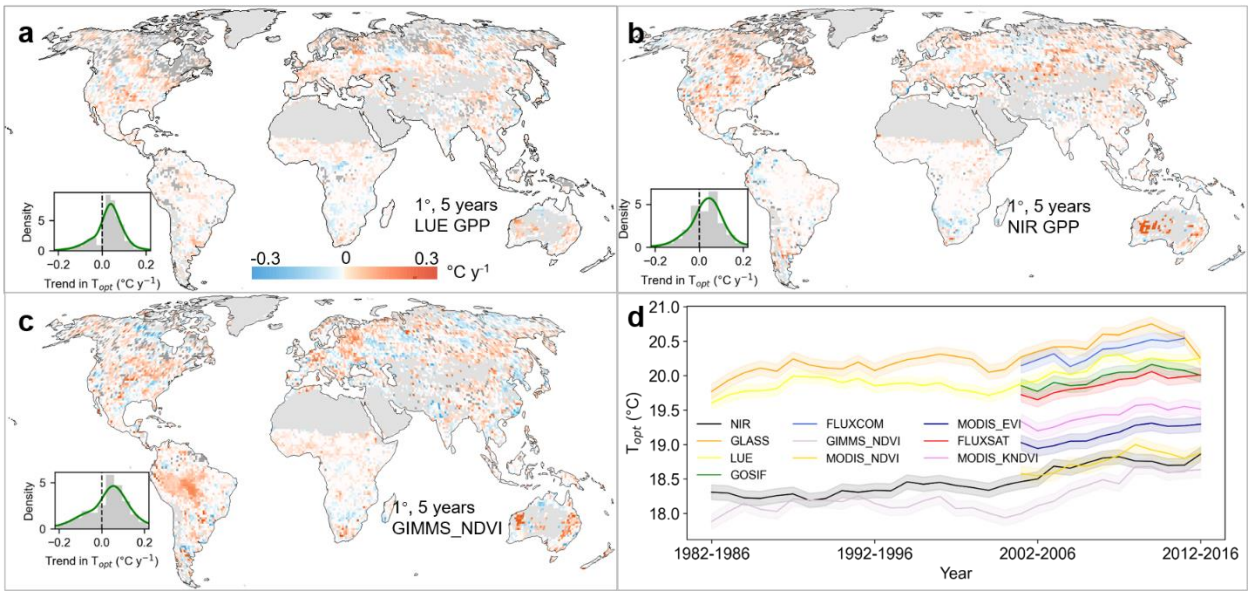

Supplementary Figure 6 | a-c, Spatial patterns of trends in T_{opt} with a 5-y temporal window and a 1° spatial window for 1982-2016 based on different vegetation growth data sets (LUE GPP, NIR GPP, and GIMMS NDVI). Light gray indicates areas with sparse or no vegetation, and dark gray indicates areas where T_{opt} could not be successfully retrieved (see Methods). **d**, Temporal dynamics of T_{opt} for different GPP data sets and vegetation index data sets with a 5-y temporal window and a 1° spatial window for 1982-2016 or 2001-2016. The solid lines indicate the dynamics of global average T_{opt}, and the shaded areas represent the 95% confidence interval of T_{opt}.

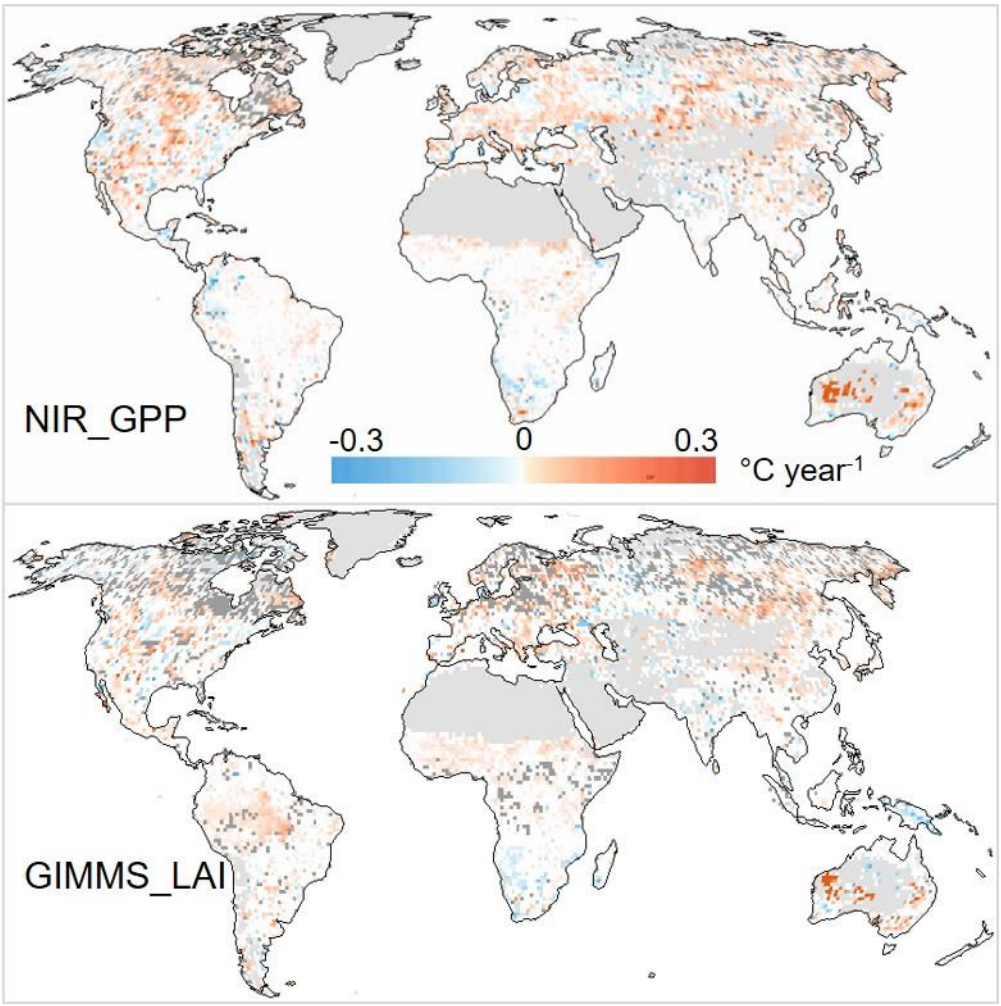

Supplementary Figure 7 | Spatial patterns of trends in Topt using different datasets for 1982-2015. LAI represents one part of decomposed GPP. Light gray indicates areas with sparse or no vegetation, and dark gray indicates areas where Topt could not be successfully retrieved (see Methods in the manuscript).

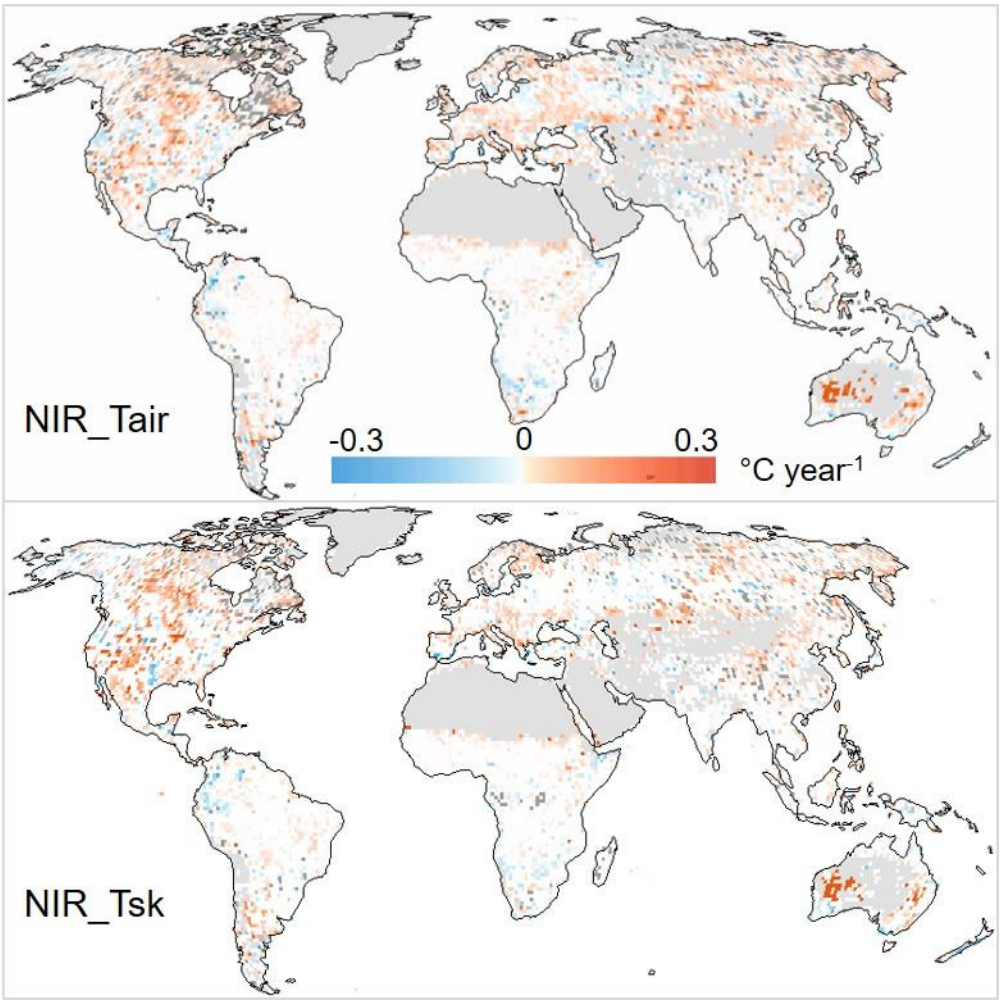

Supplementary Figure 8 | Spatial patterns of trends in Topt using different temperature datasets for 1982-2016. NIR_Tair represents the result from air temperature, and NIR_Tsk indicates the result from skin temperature (temperature of the surface of the Earth, near to leaf temperature). Light gray indicates areas with sparse or no vegetation, and dark gray indicates areas where Topt could not be successfully retrieved (see Methods in the manuscript).

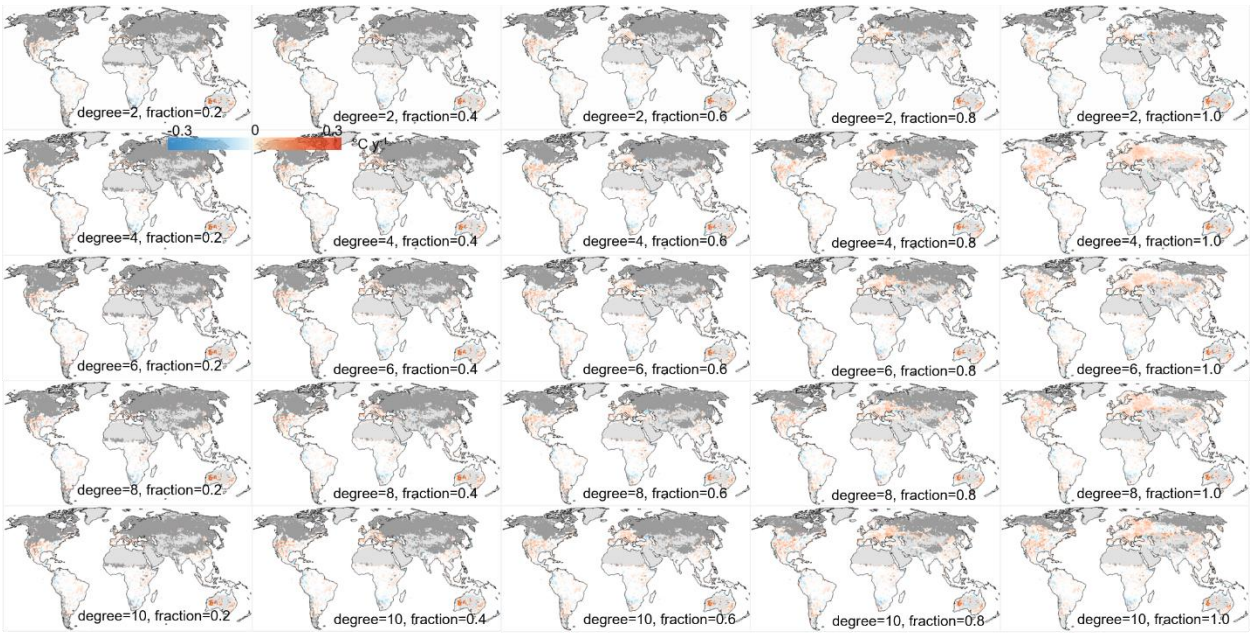

Supplementary Figure 9 | Spatial patterns of trends in T_{opt} using Loess smoothing with different combinations of degrees and fractions for 1982-2016. Light gray indicates areas with bare land or sparse vegetation, and dark gray indicates areas where T_{opt} could not be successfully retrieved (see Methods).

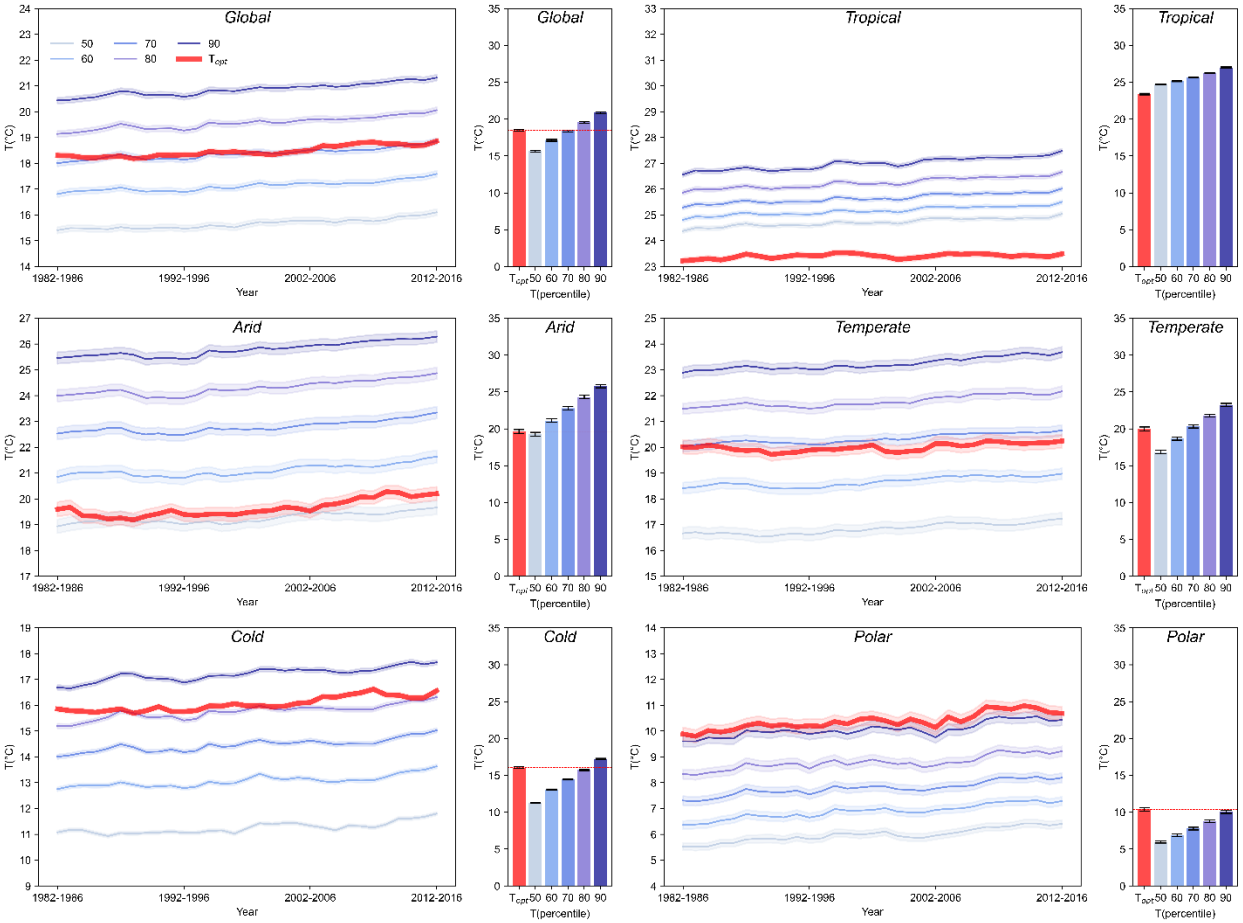

Supplementary Figure 10 | Relationships between T_{opt} and 50-90% temperature percentiles. Time series of T_{opt} and the percentiles of air temperature above 0 °C (considered as covering growing-season conditions) within a 5-y temporal window and a 1° spatial window for 1982-2016 at the global scale and for different climatic zones. The solid lines indicate the dynamics of T_{opt} (red) and the air temperature percentiles (blue), and the shaded areas indicate their 95% confidence interval. The bars and error bars indicate the mean and 95% confidence interval, respectively, of T_{opt} and the temperature percentile.

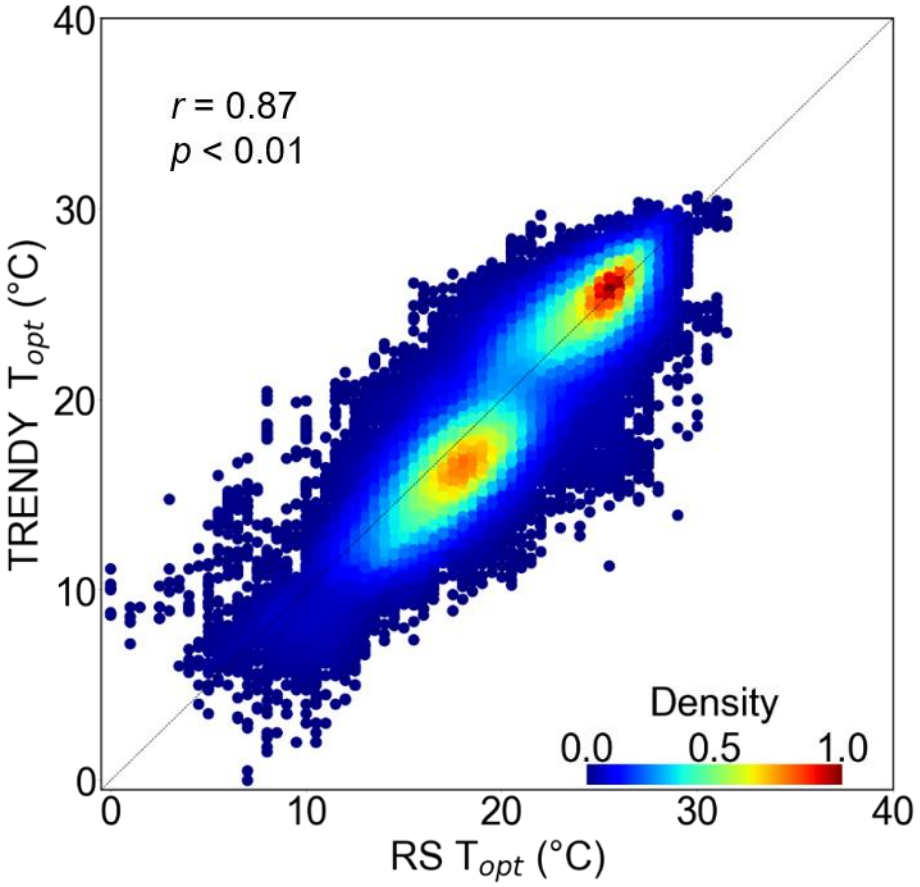

Supplementary Figure 11 | Comparison of T_{opt} derived from RS data (NIR GPP) and the TRENDY models. The RS data were resampled to 0.5° to match the spatial resolutions of the outputs from the TRENDY models. T_{opt} was derived using a 5-y temporal window and a 2.5° (5×5) spatial window for 1982-2016 for comparing satellite observations and the output of the TRENDY models.

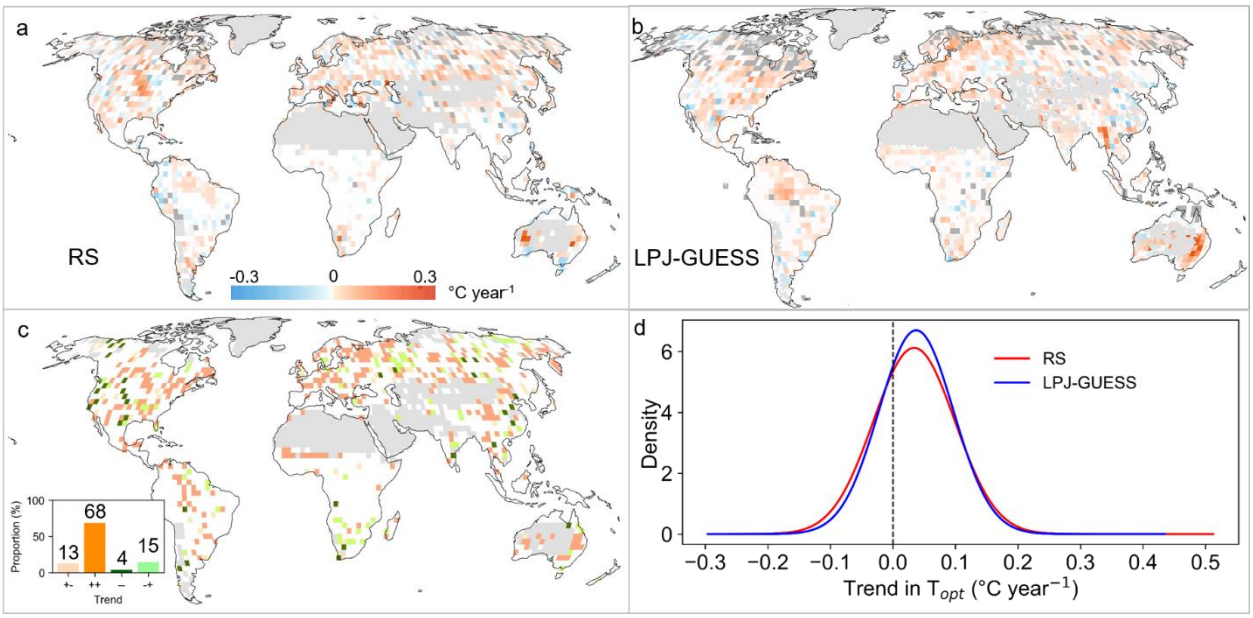

Supplementary Figure 12 | Trends in T_{opt} derived from remote sensing (RS) data (NIR GPP) (a), the LPJ-GUESS model under standard conditions (b), driven by all factors (temperature, precipitation, radiation, CO_2, and nitrogen deposition), and (c-d) the agreement in trends. The RS data were resampled to 0.5° to match the spatial resolutions of the LPJ-GUESS model. T_{opt} was derived using a 5-y temporal window and a 2.5° (5×5) spatial window for 1982 to 2016 for comparing satellite observations and the output of the LPJ-GUESS model.

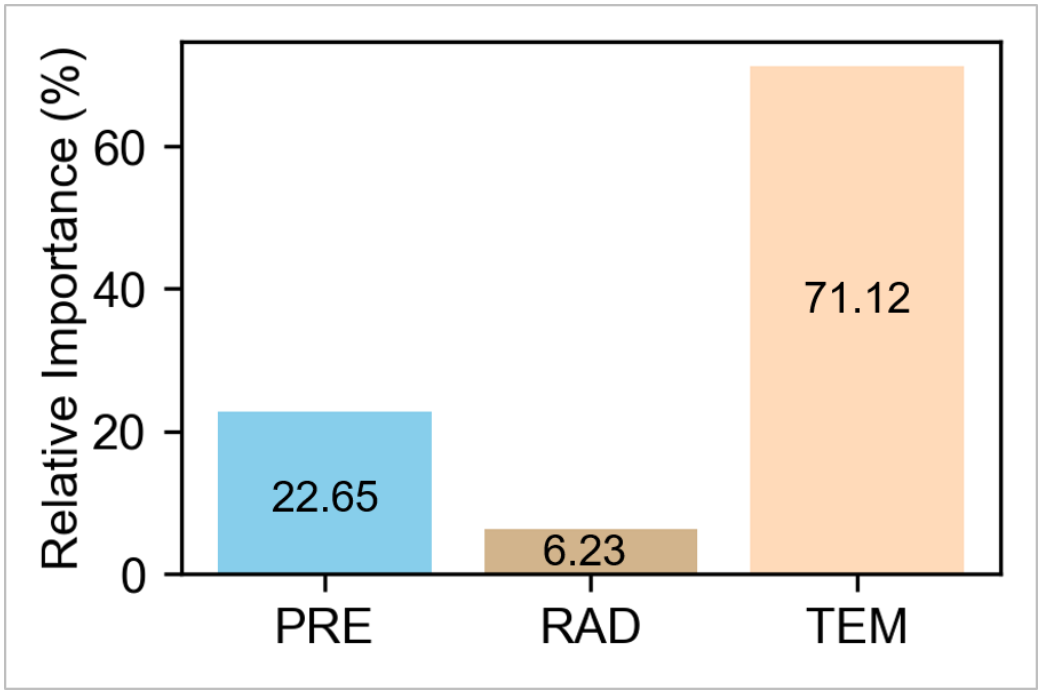

Figure 13 | Relative importance of three climatic factors (precipitation, incoming solar radiation and air temperature) for the trend in T_{opt} derived from satellite observations.

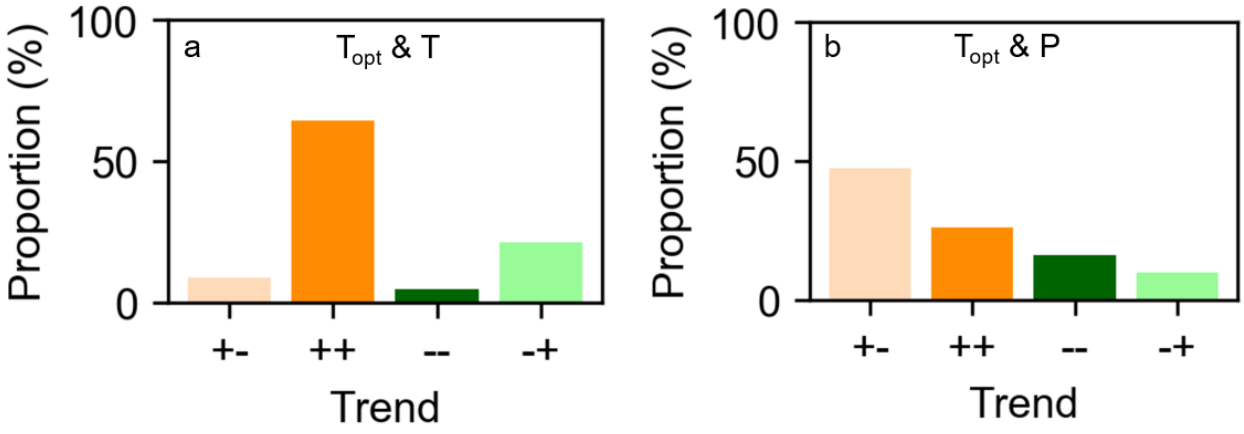

Supplementary Figure 14 | Consistency between the trend in satellite-observed T_{opt} and the trend in the 5-y moving window of mean air temperature (T) and precipitation (P) derived from the ERA5 data set. +-, increasing T_{opt} and decreasing T (or P); ++, increasing T_{opt} and increasing T (or P); --, decreasing T_{opt} and decreasing T (or P); -+, decreasing T_{opt} and increasing T (or P).

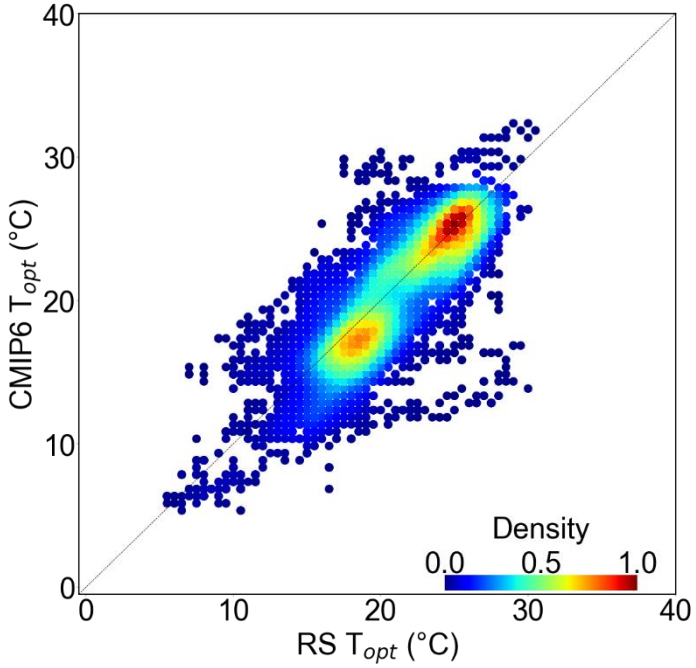

Supplementary Figure 15 | Comparison of T_{opt} derived from RS data (NIR GPP) and the CMIP6 models. The RS data were resampled to 1.0° to match the spatial resolutions of the CMIP6 model outputs. T_{opt} was derived using a 5-y temporal window and a 5.0° (5×5) spatial window for 1982-2014 for comparing satellite observations and the output of the CMIP6 models.

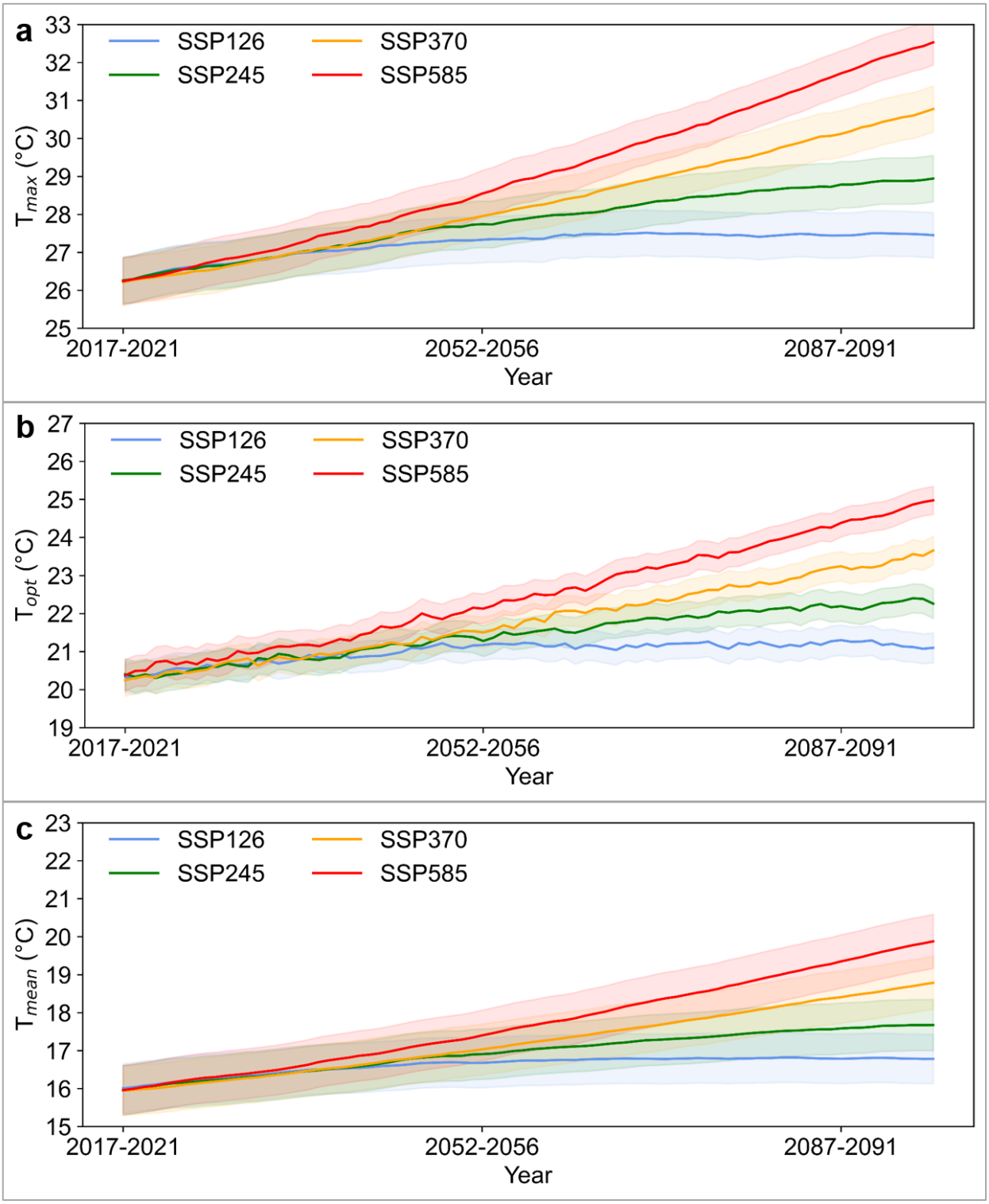

Supplementary Figure 16 | Projected temporal dynamics of (a) mean daily maximum temperature, (b) T_{opt} and (c) mean temperature for 2017-2100 under different scenarios (SSP126, SSP245, SSP370, and SSP585). T_{opt} was estimated from 23 CMIP6 models using a 5-y temporal window and a 5° spatial window for 2017-2100. The maximum and mean temperatures were calculated using the same spatio-temporal windows as for T_{opt}. The solid lines indicate the dynamics of maximum temperature, T_{opt}, and mean temperature, and the shaded areas represent the 95% confidence interval of the maximum temperature, optimal temperature, and mean temperature.

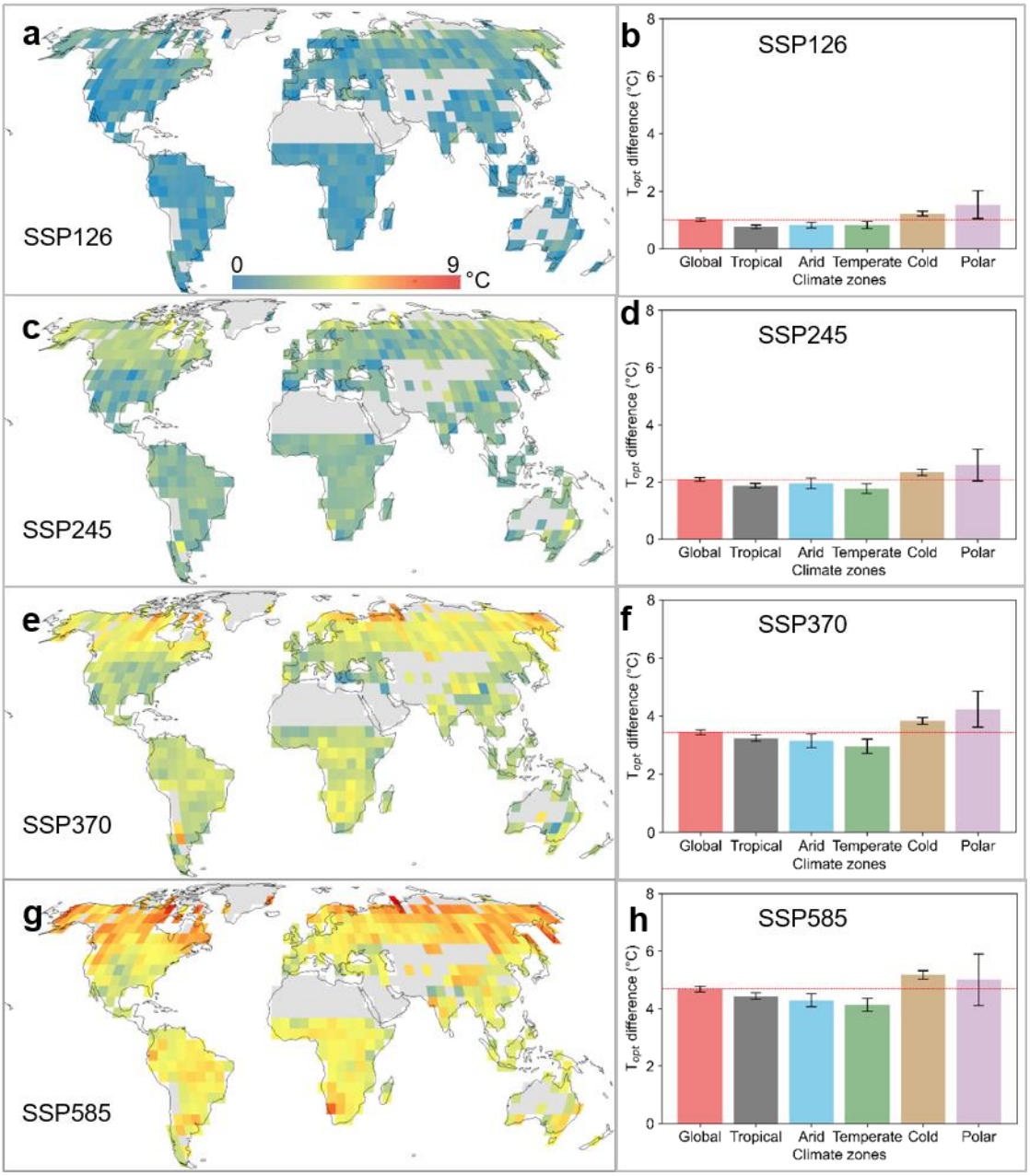

Supplementary Figure 17 | Projected changes in T_{opt} of vegetation productivity under different scenarios. **a**, **c**, **e**, and **g** are the spatial patterns of the difference in T_{opt} between two 5-y windows (2017-2021 and 2096-2100) under different scenarios. **b**, **d**, **f**, and **h** are the mean difference in T_{opt} between two 5-y windows (2017-2021 and 2096-2100) under different scenarios at the global scale and for different climatic zones. The error bars indicate the 95% confidence interval of the differences in T_{opt}. T_{opt} was estimated from 23 CMIP6 models using a 5-y temporal window and a 5° spatial window for 2017-2100.

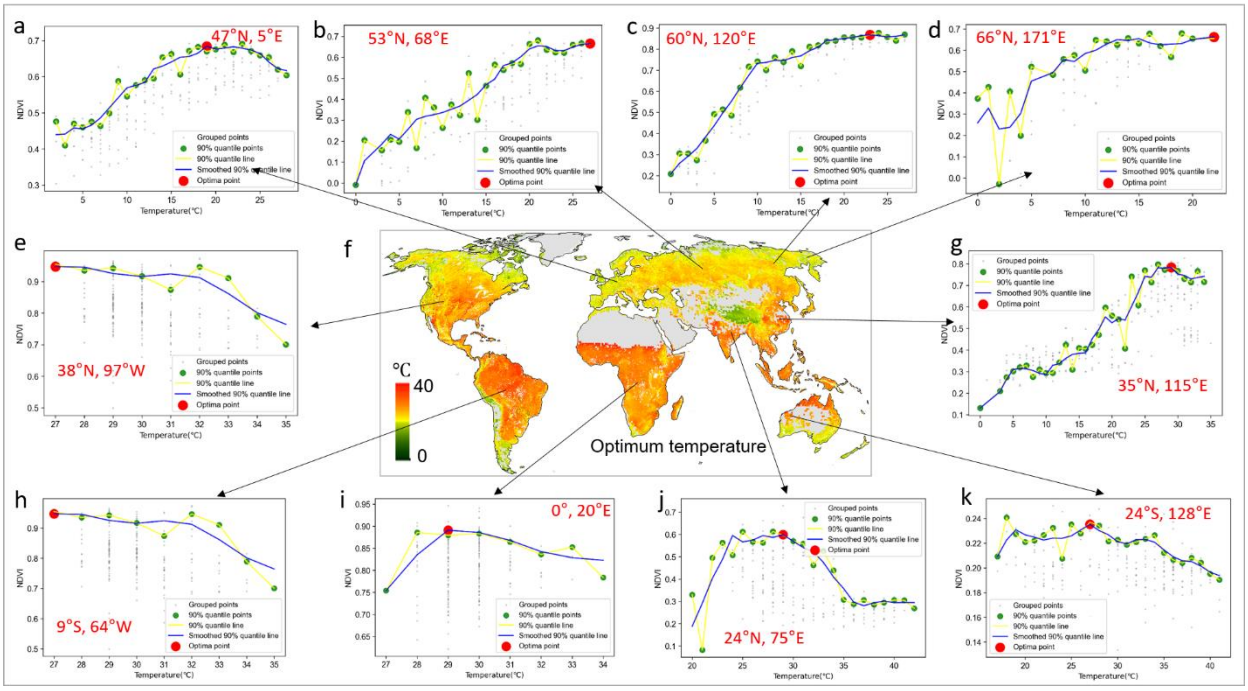

Supplementary Figure 18 | Illustrations of T_{opt} extraction using the method from Huang et al. (2019). Relationships between monthly GPP and temperature extracted from 10-y temporal window (2002-2011) but without using a spatial window. The map shows the locations of the selected sample plots, corresponding to the location of the plots in Fig. S1.

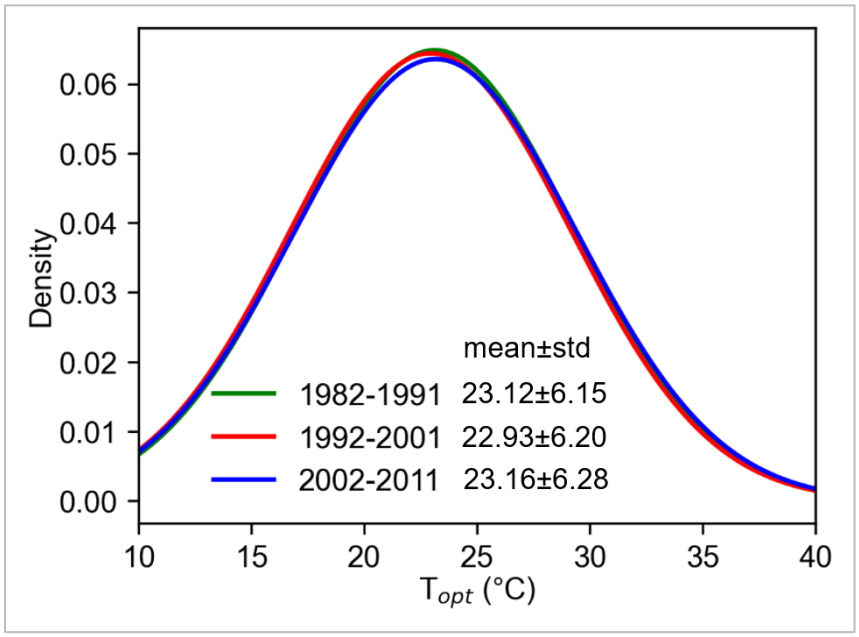

Supplementary Figure 19 | T_{opt} derived from the method of Huang et al. (2019) in three periods, 2002-2011, 1992-2001, and 1982-1991.

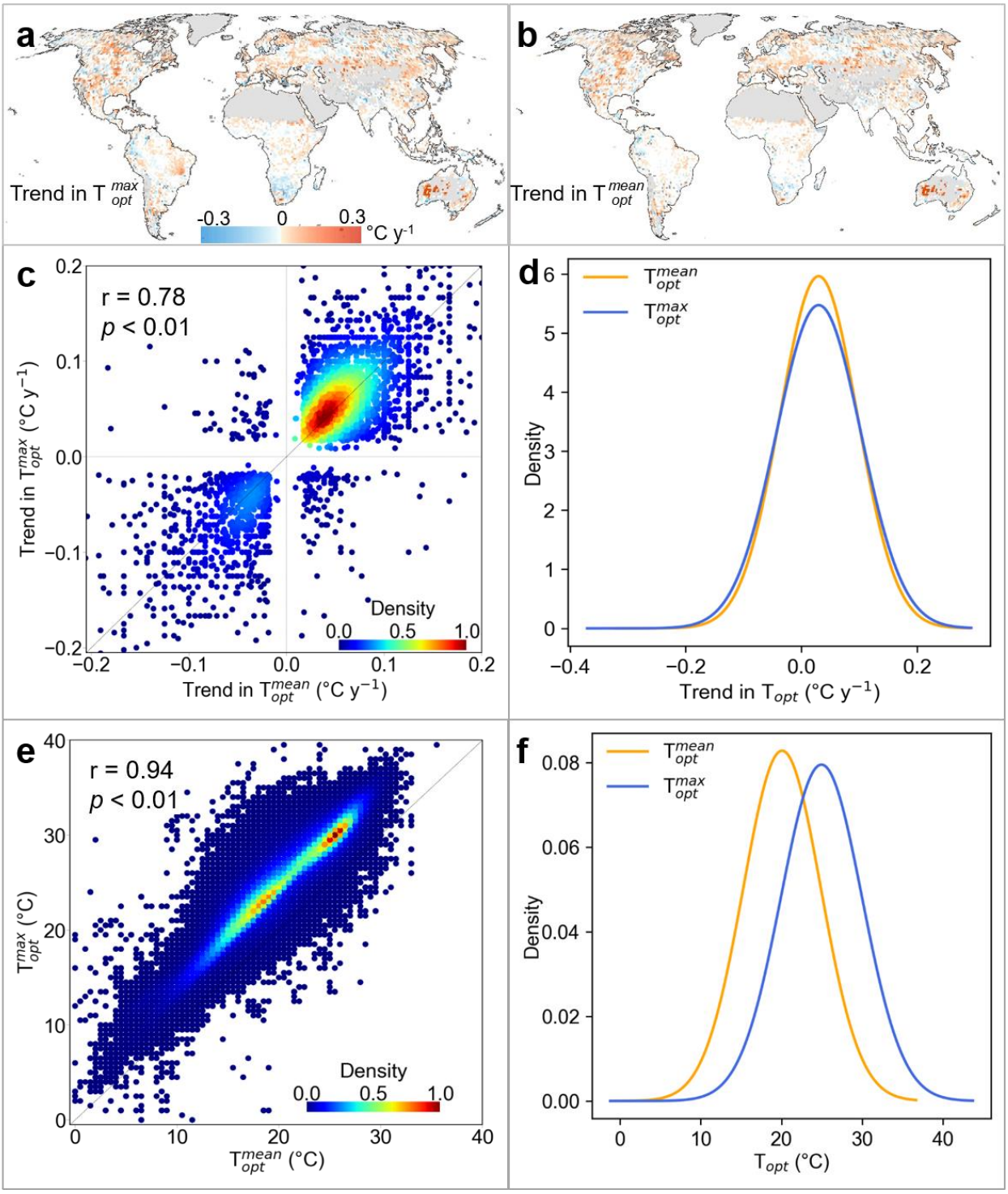

Supplementary Figure 20 | Comparison of T_{opt} derived from the monthly mean of daily maximum air temperature (T_{opt}^{max}) and from the monthly mean of daily mean air temperature (T_{opt}^{mean}) using a 5-y temporal window and a 1° spatial window for 1982-2016. Trends in T_{opt} where the temperature was extracted from (a) maximum daily air temperature and (b) mean daily air temperature. (c) Scatterplot of the correlations of trends in T_{opt}^{mean} and T_{opt}^{mean}, and (d) the density distribution. (e) Differences in T_{opt}^{max} and T_{opt}^{mean} for 1982-2016 and (f) their density distributions.

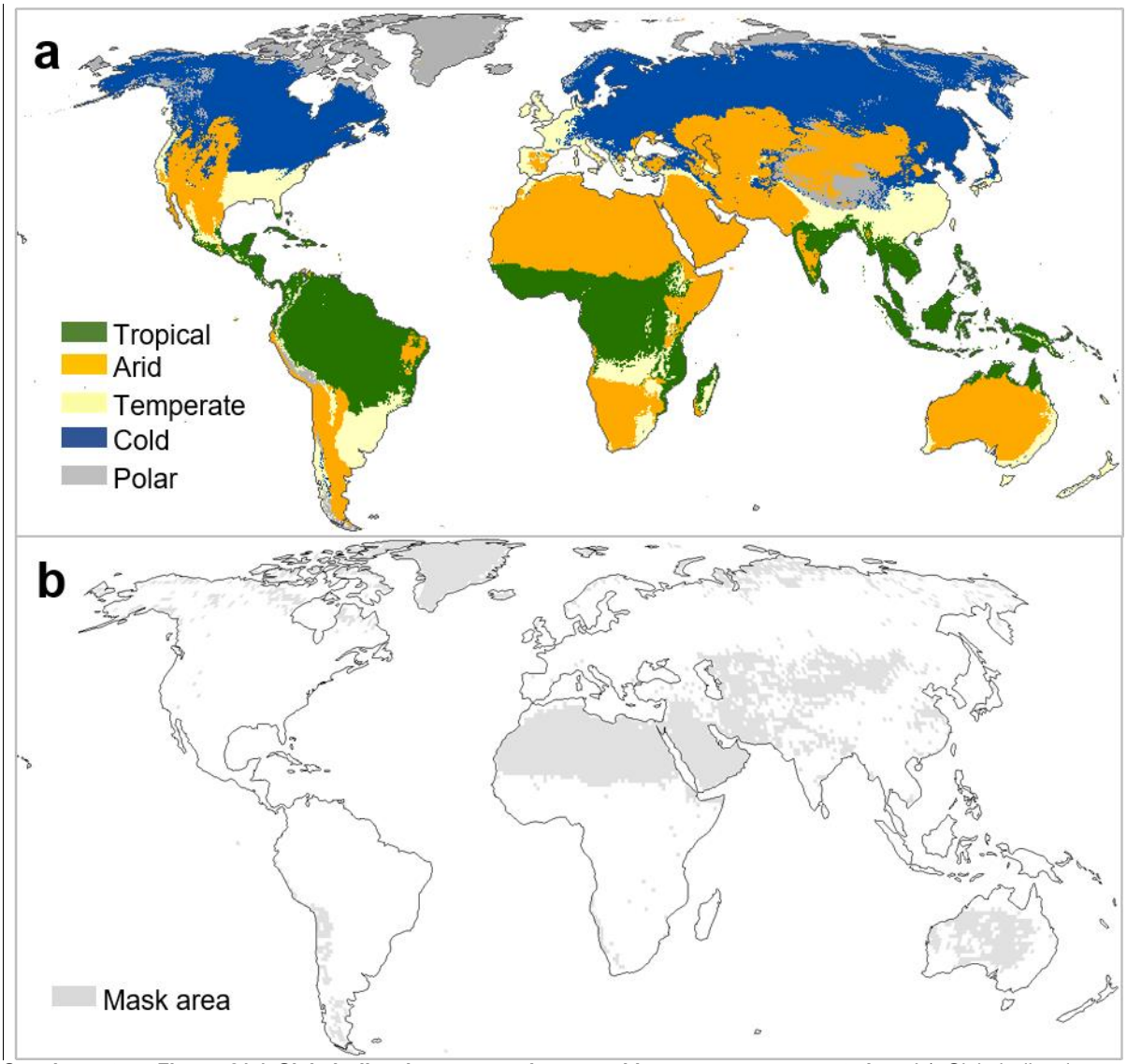

Supplementary Figure 21 | Global climatic zones and areas with sparse or no vegetation. (a) Global climatic zones at 1/12°spatial resolution (Beck et al., 2018). (b) Global land cover in 2000, with irrigated cropland and sparse or no vegetation derived from the land-cover data product of the ESA climate change initiative at 1° spatial resolution.

Supplementary Table 1. Vegetation proxy data sets and climate data sets used in this paper.

Data	Temporal coverage	Temporal resolution	Spatial resolution
NIR GPP	1982-2018	Monthly	0.05°
GMMMIS NDVI	1982-2016	15-d	1/12°
GMMMIS LAI	1982-2015	15-d	1/12°
MODIS NDVI/EVI/KNDVI	2001-2020	Monthly	0.05°
GLASS GPP	1982-2018	Monthly/8-d	0.05°
Improved LUE-GPP	1982-2016	Monthly	1/12°
GOSIF GPP	2001-2020	8-d	0.05°
FLUXSAT GPP	2001-2020	Daily	1/12°
FLUXCOM GPP	2001-2015	Monthly	1/12°
ERA5 T, P, and R	1979-2020	Monthly	0.1°
CRU T	1901-2020	Monthly	0.5°

Note: T = temperature; P = precipitation; R = radiation

Supplementary Table. 2. Information about FLUXNET2015 sites used in this study.

SITE_ID	SITE_NAME	IGBP	Latitude	Longitude	Elevation
AU-Tum	Tumbarumba	EBF	-35.6566	148.1517	1200
BE-Bra	Brasschaat	MF	51.3076	4.5198	16
BE-Vie	Vielsalm	MF	50.3049	5.9981	493
CA-Oas	Saskatchewan - Western Boreal, Mature Aspen	DBF	53.6289	-106.1978	530
CA-Obs	Saskatchewan - Western Boreal, Mature Black Spruce	ENF	53.9872	-105.1178	628.94
CA-TP3	Ontario - Turkey Point 1974 Plantation White Pine	ENF	42.7068	-80.3483	184
CA-TP4	Ontario - Turkey Point 1939 Plantation White Pine	ENF	42.7102	-80.3574	184
CH-Lae	Laegern	MF	47.4783	8.3644	689
CZ-BK1	Bily Kriz forest	ENF	49.5021	18.5369	875
DE-Hai	Hainich	DBF	51.0792	10.4522	430
DE-Lnf	Leinefelde	DBF	51.3282	10.3678	451
DK-Sor	Soroe	DBF	55.4859	11.6446	40
FR-LBr	Le Bray	ENF	44.7171	-0.7693	61
FR-Pue	Puechabon	EBF	43.7413	3.5957	270
IT-Lav	Lavarone	ENF	45.9562	11.2813	1353
IT-Noe	Arca di Noe - Le Prigionette	CSH	40.6062	8.1517	25
IT-Ren	Renon	ENF	46.5869	11.4337	1730
IT-Ro2	Roccarespampani 2	DBF	42.3903	11.9209	160
IT-SRo	San Rossore	ENF	43.7279	10.2844	6
RU-Cok	Chokurdakh	OSH	70.8291	147.4943	48
US-Me2	Metolius mature ponderosa pine	ENF	44.4526	-121.5589	1253
US-NR1	Niwot Ridge Forest (LTER NWT1)	ENF	40.0329	-105.5464	3050
US-SRM	Santa Rita Mesquite	WSA	31.8214	-110.8661	1120
US-Ton	Tonzi Ranch	WSA	38.4309	-120.966	177
US-Var	Vaira Ranch- Ione	GRA	38.4133	-120.9508	129
US-	Willow Creek	DBF	45.8059	-90.0799	520

WCr					
US-Wkg	Walnut Gulch Kendall Grasslands	GRA	31.7365	-109.9419	1531

Supplementary Table 3. TRENDY model simulations under different scenarios.

Scenarios	CO_2	Climate	Land cover	Labels
S0	0	0	0	-
S1	**1**	0	0	CO_2
S2	**1**	**1**	0	CO_2+CL
S3	**1**	**1**	**1**	CO_2+CL+LC, standard scenario
S2-S1	0	**1**	0	CL
S3-S2	0	0	**1**	LC

Note: 0, constant value (monthly recycling mean and variability from 1901 to 1920); 1, varying value. CL=climate; LC=land cover.

Supplementary Table 4. LPJ-GUESS model simulations under different scenarios.

Scenarios	Temperature	Precipitation	Radiation	CO2	Nitrogen deposition
ALL	**1**	**1**	**1**	**1**	**1**
TEM	**1**	0	0	0	0
PRE	0	**1**	0	0	0
RAD	0	0	**1**	0	0
CO2	0	0	0	**1**	0
NDE	0	0	0	0	**1**

Note: 0, constant value (monthly recycling mean and variability from 1901 to 1920); 1, varying value.

Supplementary Table 5. Name, spatial resolution and source of origin of the 23 CMIP6 models used.

Model name	Spatial resolution	Modeling center
ACCESS-ESM1-5	1.2414° × 1.8750°	Commonwealth Scientific and Industrial Research Organization and Bureau of Meteorology, Australia
BCC-ESM1	2.8125° × 2.8125°	Beijing Climate Center, China Meteorological Administration, China
BCC-CSM2-MR	0.25 ° ×0.25°	Beijing Climate Center, China Meteorological

		Administration, China
CanESM5	2.8125° × 2.8125°	Canadian Center for Climate Modeling and Analysis (CCCma), Canada
CanESM5-CanOE	2.8125° × 2.8125°	Canadian Center for Climate Modeling and Analysis (CCCma), Canada
CAS-ESM2-0	1.40625° × 1.40625°	Chinese Academy of Sciences, China
CESM2-WACCM	0.9375 ° ×1.25°	National Center for Atmospheric Research, Climate and Global Dynamics Laboratory, USA
CMCC-CM2-SR5	0.9375 ° ×1.25°	Fondazione Centro Euro-Mediterraneo sui Cambiamenti Climatici, Italy
CMCC-ESM2	0.9375 ° ×1.25°	Euro-Mediterranean Center on Climate Change, Italy
CNRM-CM6-1	1.40625° ×1.40625°	National Center for Meteorological Research, France
CNRM-ESM2-1	1° ×1°	National Center for Meteorological Research, France
E3SM-1-1	1° ×1°	Lawrence Livermore National Laboratory, USA
E3SM-1-1-ECA	1° ×1°	Lawrence Livermore National Laboratory, USA
EC-Earth3-Veg	0.703125° ×0.703125°	State Meteorological Agency, Spanish
GFDL-ESM4	1° ×1.25°	Geophysical Fluid Dynamics Laboratory/NOAA, USA
INM-CM4-8	1.5° ×2.0°	Institute for Numerical Mathematics (INM), Russia
INM-CM5-0	1.5° ×2.0°	Institute for Numerical Mathematics (INM), Russia
IPSL-CM6A-LR	1.26° ×2.50°	Institut Pierre Simon Laplace (IPSL), France
MIROC-ES2L	2.8125° × 2.8125°	Japan Agency for Marine-Earth Science and Technology, Japan
MPI-ESM-1-2-HAM	0.9375° ×0.9375°	ETH Zurich, Switzerland
NorESM2-LM	1.875° × 2.5°	Norwegian Meteorological Institute, Norway
NorESM2-MM	0.9375° × 1.25°	Norwegian Meteorological Institute, Norway
UKESM1-0-LL	1.25° × 1.875°	Met Office Hadley Centre, UK

References

Beck, H. E., Zimmermann, N. E., McVicar, T. R., Vergopolan, N., Berg, A., & Wood, E. F. (2018). Present and future Koppen-Geiger climate classification maps at 1-km resolution. *Sci Data, 5*, 180214. doi:10.1038/sdata.2018.214

Huang, M., Piao, S., Ciais, P., Penuelas, J., Wang, X., Keenan, T. F., . . . Janssens, I. A. (2019). Air temperature optima of vegetation productivity across global biomes. *Nat Ecol Evol, 3*(5), 772-779. doi:10.1038/s41559-019-0838-x